# Microseismicity observation and characterization at Cape Modern and Utah FORGE

Nori Nakata<sup>1</sup>, Sin-Mei Wu<sup>1</sup>, Chet Hopp<sup>1</sup>, Michelle Robertson<sup>1</sup> and Sireesh Dadi<sup>2</sup>

<sup>1</sup>Earth and Environmental Sciences Area, Lawrence Berkeley National Laboratory, 1 Cyclotron Rd., Berkeley, CA 94720

<sup>2</sup>Fervo Energy, Houston, TX 77002

nnakata@lbl.gov

**Keywords:** seismic monitoring, microseismicity, Cape Modern, Utah FORGE

#### **ABSTRACT**

To prepare the new stimulation and exploration of geothermal resources at Cape Modern, Utah, we deploy seis mometers, test noise level, and refine velocity models. Shallow boreholes (a few tens of meters) help to improve the signal-to-noise ratio compared to the sensors at the ground surface. Background seismicity before stimulation with the new seismometers is mostly concentrated on the east of the array, which is outside of the geothermal field. To better characterize seismicity and fractures, moment tensor is important in addition to the detection and location of the events. We develop a method to better characterize microseismic events and revisit stimulation data at Utah FORGE to test it before having the data at Cape Modern. A few deep borehole geophones can detect small events very well, but because of the limited coverage of the aperture, estimation of focal mechanisms is challenging. The surface nodal sensors are useful to compensate the aperture coverage but only for larger events. We will present focal mechanism estimation for smaller events by combining both surface and deep borehole measurements. These methods can be used for stimulation at the Cape Modern site to better characterize small events.

## 1. INTRODUCTION

Understanding the detailed stress and strain states in the reservoir and surrounding structure is crucial for mitigating large induced seismicity and reservoir management in geothermal fields. This is especially important when we increase the usage of geothermal resources and employ enhanced geothermal systems (EGS). We consider that there are two key factors to characterize subsurface stresses; densification of seismic monitoring sensors and earthquake moment tensor. In this study, we present our recent work of deploy ment of seismic monitoring sensors at the Cape Modern geothermal field, which will be stimulated and thereafter as a plan. We also develop a velocity model for the field to better estimate the locations and characterization of seismicity. The velocity model will be finely tuned once we observe seismicity related to the stimulation. Before stimulation, we also deploy surface nodal networks to further densify the seismic stations. Then we demonstrate the capability of estimation of moment tensors of small earthquakes. Because we do not record seismic data at the Cape Modern site yet, we use data recorded in Utah FORGE in 2022, which is a field just next to the Cape Modern. Combination of surface and borehole seismic sensors is powerful to detect small events as well as estimating the polarity of first arrivals, which are used for moment tensor inversion. Here, we summarize our work of seismic monitoring system in Section 2 and moment tensor estimation in Section 3.

## 2. SEISEMIC MONITORING SYSTEM

#### 2.1 Shallow-borehole seismometers

Six new seismic monitoring stations were installed at the Cape Modern site aimed at complementing the extensive, preexisting monitoring network of the Univerity of Utah Seismograph Stations, in collaboration with the Utah FORGE site (Figure 1). Five of the sensors are installed in shallow (~40 m deep) boreholes, and the other is installed in a ~1 m deep posthole. All six sensors are 3-component, low-noise optical accelerometers manufactured by Silicon Audio and ASIR Seismic (who package the downhole sondes; Figure 1). They have a nominal sensitivity of 60 V/g, a dynamic range of 172 dB, and a passband from 0.005 to 1500 Hz (per manufacturer specifications; Hopp et al., 2022). Data from these stations are streamed to the EarthScope DMC in real time over the cell network and are archived under the network code 6K.

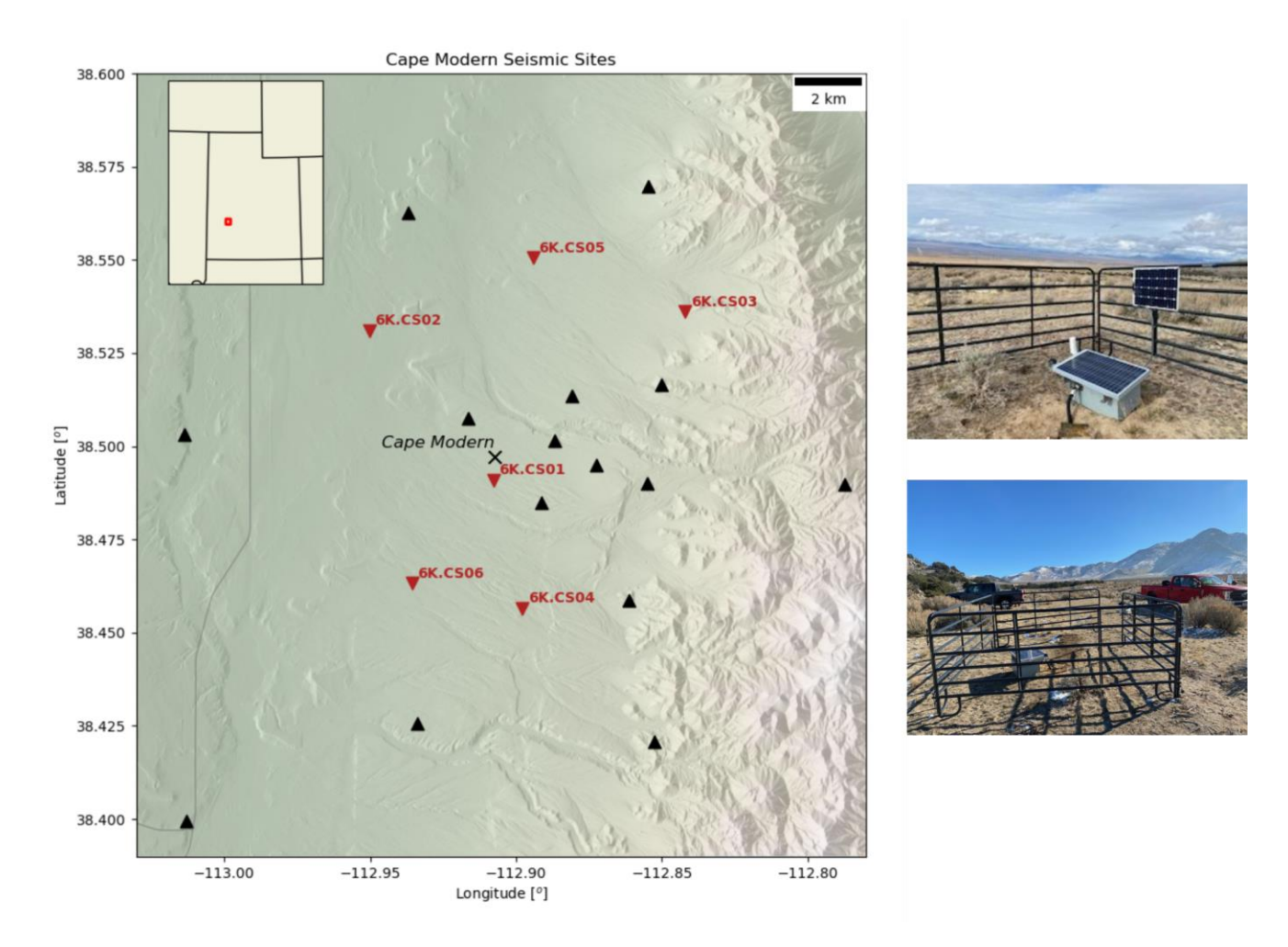


Figure 1: Map of six new seismic monitoring stations.

## 2.2 Realtime processing

Data from the new sensors, as well as all UUSS stations within ~50 km of the Cape Modern site, are ingested into an LBNL-hosted seiscomp server (Helmholtz, 2008) in near-real-time via seedlink protocol. Phase arrivals are picked via STA/LTA, refined via an AIC-based repicker, and associated and relocated using a proprietary seiscomp package (scanloc) based on the DBSCAN algorithm. Preliminary locations are estimated within a laterally continuous 1D layer cake model by the LOCSAT program. Solutions falling within 25 km of the Cape Modern site are then relocated with NonLinLoc and HypoDD within a newly developed 3D model (see next subsection). In realtime, HypoDD is run in "single-event" mode, meaning that each newly detected event is relocated relative to all other events in the catalog, whose locations are fixed. Periodically, the entire background catalog is updated by running the scrtdd package (HypoDD wrapper) on the entire catalog (Scarabello & Diehl, 2023).

### 2.3 3D velocity model

A number of studies by the FORGE team have focused on the development of a three-dimensional velocity model (most recently Zhang and Pankow, 2021). To fully cover the proposed extent of future geothermal development, however, the geographic area covered by these models needed to be expanded. Using several geophysical datasets compiled by both the FORGE team as well as Fervo Energy, here we present a preliminary, spatially expanded 3D model for the Cape Modern site.

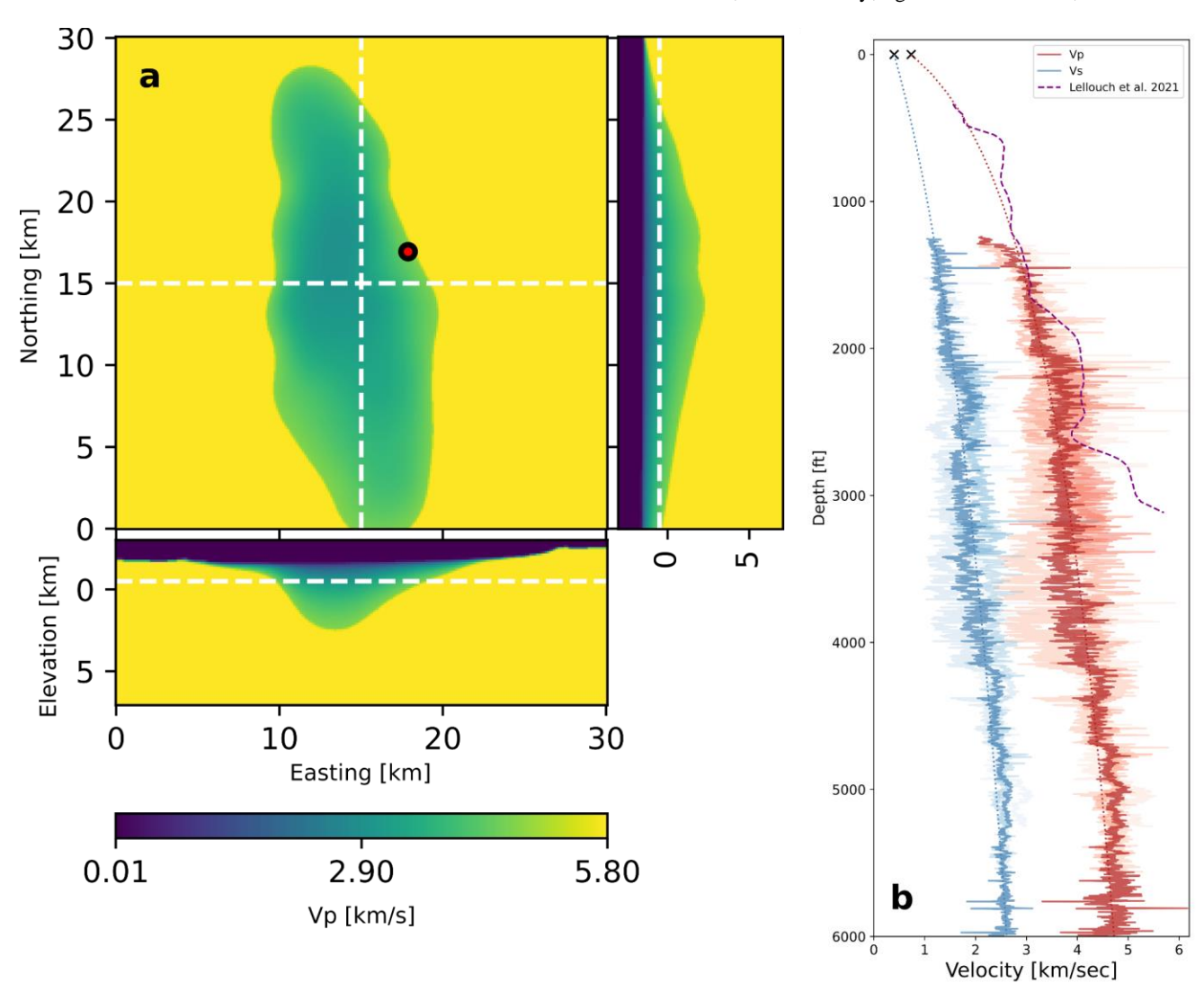


Figure 2: a) Map view and two cross sections of a new Vp model for the Cape Modern site. The dot indicates the approximate location of the Cape Modern site. b) Gray lines represent P-wave sonic logs for three Fervo wells and Forge well 58-32 at depths above the granitic basement. The red line shows the 50-ft smoothed mean of all four logs. The best fit logarithmic growth curve to the mean velocity curve is shown in dotted purple and the Vp model of Lellouch et al. (2021) is shown in dashed blue. Vp estimated from Vs30 (736 m/s; Zhang and Pankow, 2021) anchors the surface of the model and is shown as a black x.

The model presented here is 30 km square and 10 km deep (from a maximum altitude of 3000 m) with uniform 50 m grid node spacing (Figure 2a). It is defined by two surfaces, the topography as taken from the ½ arc second <u>USGS 3D Elevation Program</u>, and a surface defining the top of basement rock (typically granite where directly sampled). The top-of-basement surface was defined by Fervo through a combination of 3D seismic lines shot by the FORGE team and Fervo, FORGE and Fervo gravity surveys of the basin, and FORGE and Fervo well logs for boreholes drilled into basement rock. The spatial extent of this surface was extrapolated to the limits of the desired final model and clipped at the topography surface where the extrapolation exceeded ground elevation. In the southern portion of the basin, the extrapolation did not adequately reflect the outcropping of basement rock at the Mineral Mountains' range bounding fault, which forced us to include a vertical discontinuity where the range meets the basin fill. More work should be undertaken to better smooth this section of the model but it is unlikely to affect simple uses such as raypath solvers.

Above the ground surface, the seismic velocities are set to 0.01 km/s while below the top-of-basement surface a constant P-wave velocity of 5.8 km/s was applied, which is consistent with the speed measured by sonic logging at basement depths across the study area. Inside the basin, we fit a logarithmic function to the mean P-wave sonic velocity measured in the three Fervo well logs and Forge well 58-32 (Figure 2b). Well log velocities are ignored below the contact with the granitic basement. The one condition imposed on this fit was that the function be anchored to Vs30=400 m/s, estimated by Zhang and Pankow (2019). The VpVs profile of Lellouch et al. (2021) estimated a VpVs ratio of 1.84 for the shallowest 100 m of well 78-32, so we anchor the logarithmic function to Vp=736 m/s at the surface. The function takes the form:

$$Vp = 1.46 * ln(6.7x + 0.86) + 0.95$$

where x is depth in kilometers and Vp is in km/s.

A constant Vp/Vs ratio of 1.71 was applied to the basement granite, while a depth dependence was modeled for Vs in the basin. Following the velocity profiles of Lellouch et al. (2021) and personal communication with Peter Niemz, we fit a quadratic function to the Vp/Vs ratio of Lellouch et al. (2021) and stretched it to fit the full basin depth of the model at each given easting/northing coordinate, finally dividing these values into the Vp model to arrive at the final Vs model.

#### 3. MOMENT TENSORESTIMATION

To understand the capability of estimating microseismicity moment tensor (MT) with passive monitoring system and to develop methods for the upcoming stimulation at Cape Modern, we revisit the stimulation data recorded in 2022 at Utah FORGE an adjacent site.

#### 3.1 Seismic Catalog and Data at Utah FORGE

In April 2022, three phases of stimulation were operated at Utah FORGE. The manually relocated seismic catalog associated with the stimulation contains 7431 events with magnitudes ranging from -2 to 0 (Dyer et al., 2023). Event locations are confined within a few hundred meters from the stimulation locations along well 16A at depths around 2500 meters (Figure 3). The concurrent passive seismic monitoring system was consisted of a dozen of downhole geophones and a ~200-geophone surface array. Downhole geophones emplaced within well 58 and well 78B have high quality and complete recording during the stimulation and hence we focus on them for the analyses in this study. Surface nodal array is consisted of 13 subarrays, where each subarray is formed as four-by-four geometry with a spacing of around 30 meters (Figure 3).

Microseismicity recorded at downhole geophones generally have high signal-to-noise ratio (SNR) at the cataloged magnitudes, likely related to its low-noise environment and the sensors were deployed close (<1 km) to the hypocenter. On the other hand, the surface array was generally >2.5 km away deployed on the sediment layer, which causes high attenuation of signals and only events larger than M0 are recorded with reasonable SNR even after stacking across the entire 16 elements of each subarray (Figure 4). For the goal of MT estimation, the surface array is essential owing to its excellent azimuthal coverage relative to the main seismically-active zone. In the following section, we explore signal processing techniques to enhance incoming *P*-wave energy in order to retrieve its polarity and amplitude for lower magnitude events.

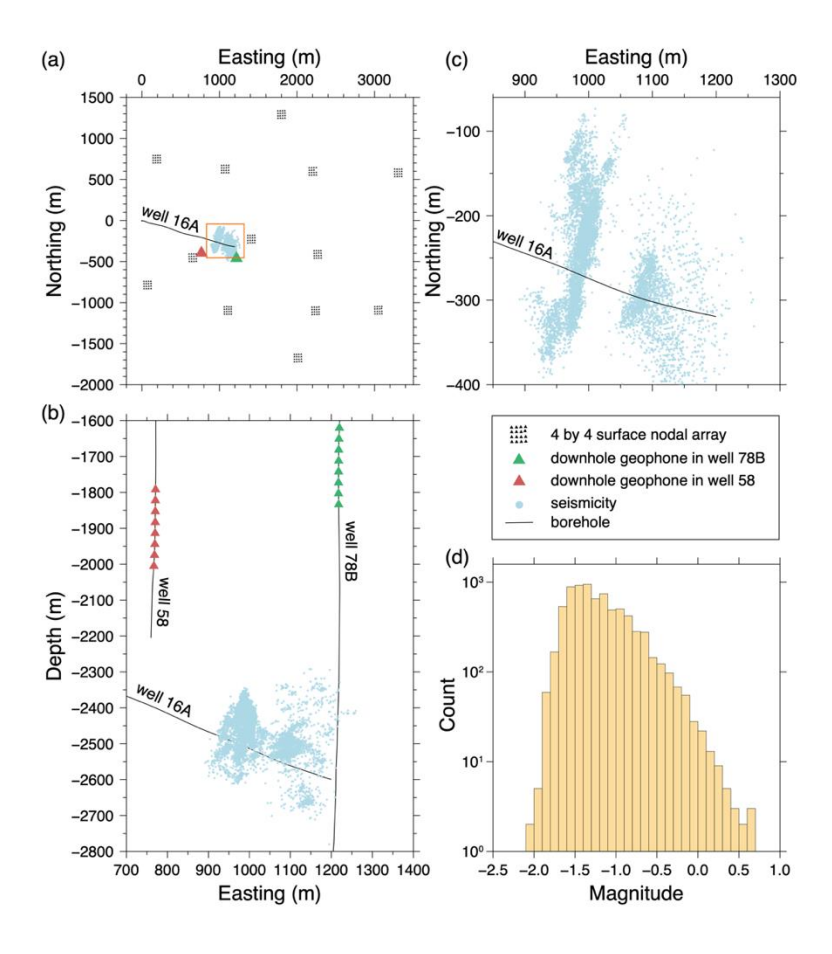


Figure 3: Illustration of seismic arrays (triangles), seismicity (dots), and borehole geometry (lines) at Utah FORGE. (a) An overall mapview showing relative distribution of surface arrays and main seismically-active area (orange square). (b) An enlarged depth cross-section showing downhole geophones and seismicity. (c) An enlarged area of mapview corresponding to the orange square in (a). (d) Frequency-Magnitude distribution based on the seismic catalog of 2022 April stimulation (Dyer et al., 2023).

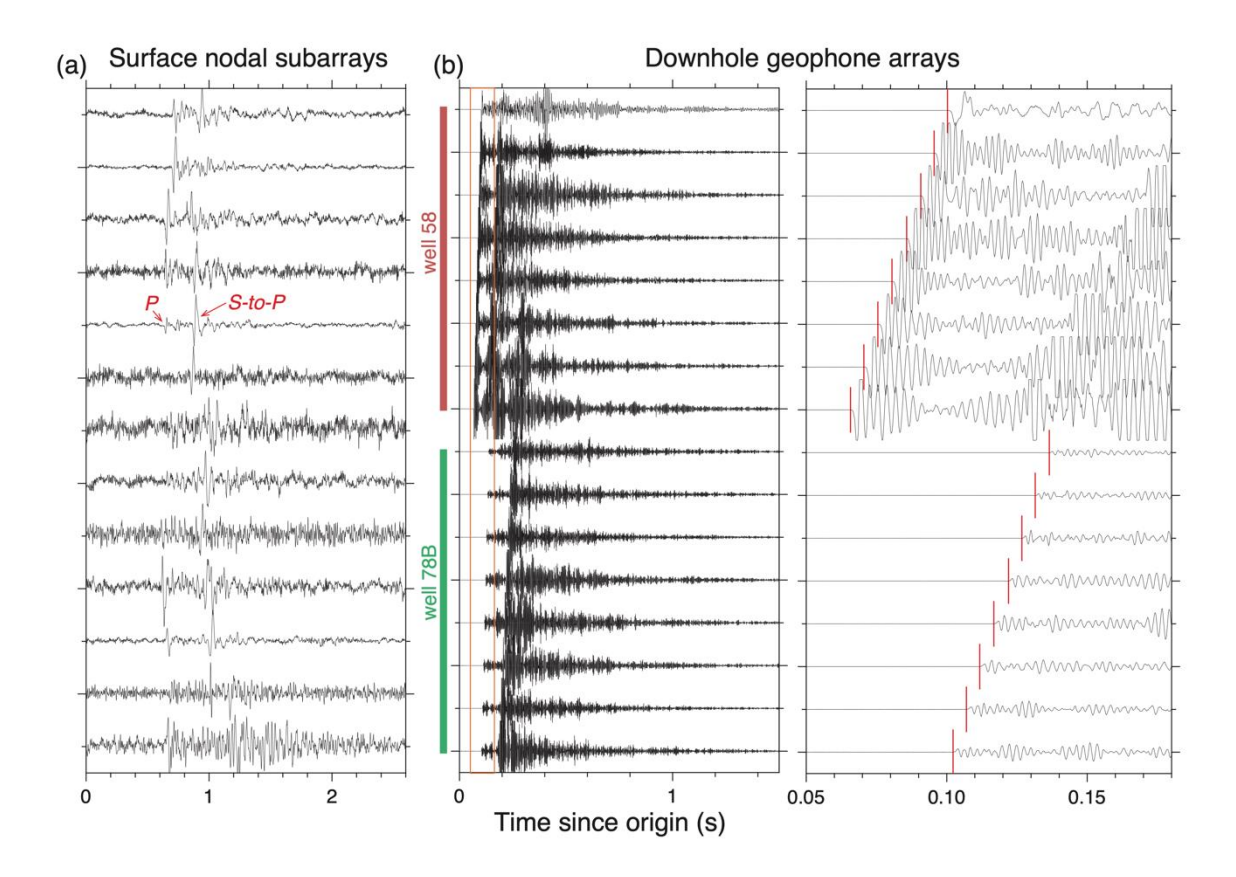


Figure 4: Examples of seismic signals from a M0.38 event on April 21 (2022-04-21T16:10:57). (a) Linearly-stacked waveforms of vertical component across 16 elements at each of the surface nodal subarrays. (b) (left) Vertical component of downhole geophone and (right) the enlarged window focusing on the first arrivals corresponding the orange rectangle on the left. The red bars are the onset picks based on SNR detection.

## 3.2 Array Processing and Polarity and Amplitude Determination

For each of the surface subarray, instead of linear stacking, we apply beamforming to account for the incoming P energy from various directions. Assuming an incoming direction, the beamforming technique allows to search the phase differences at vertical component among array elements by shifting and stacking that maximize the coherent energy across the array (Nakata et al., 2015). As we observe prominent S-to-P phase closely follows the P phase (Figure 4), to avoid contamination from the phase potentially from different incoming direction, we exclusively focus on the P wave window by muting the signals approximately 0.1 second after. The characteristic frequency filtered for the analysis is between 10 and 100 Hz. In addition, we apply a noise-suppression filter to further enhance the coherent signals across the array and retain their amplitude before stacking (Nakata et al., 2015).

The result in Figure 5 shows substantial improvement in direct P signals, where the first arrivals from event magnitudes as low as M-0.3 can be clearly identified. We manually pick the onset time as a reference time to further retrieve the first motion polarity and amplitude. The polarity is determined by the median amplitude of vertical displacement records within a window of 20 ms following the onset time. And the amplitude is the maximum amplitude of the sum of 3-component recording within a window of 50 ms following the onset time. We note that the applied signal processing enhances the major coherent signals but may introduce inaccuracies for precise picking for the onset timing. Nonetheless, our interest is to focus on the polarity and the amplitude from the first motion, both of which information are preserved and not biased by the onset uncertainty. After manual inspection, we take 30 events that have reliable first-motion information from 7 out of 13 subarrays for MT estimation.

For downhole geophone data, we perform an SNR detection (SNR>0.01) for determining the onset time. The noise level is defined by the mean amplitude within the first 10 ms after event origin time, and the signal level is the maximum amplitude within a 5-ms window with the time mark at the end of the window. The SNR is applied to the sum of the 3-component recording from the downhole geophone records. We emphasize again that the onset time is an approximate reference for identifying first motion, which is different from the required accuracy for location purposes. Our SNR detection results are further validated by visual screening (Figure 4b). We adapt the same method from the one applied to surface array to retrieve *P* polarity and amplitude, with slight modifications of window lengths of 2 ms and 5 ms for polarity and amplitude, respectively. The 5-ms window length is based on Dyer et al. (2023).

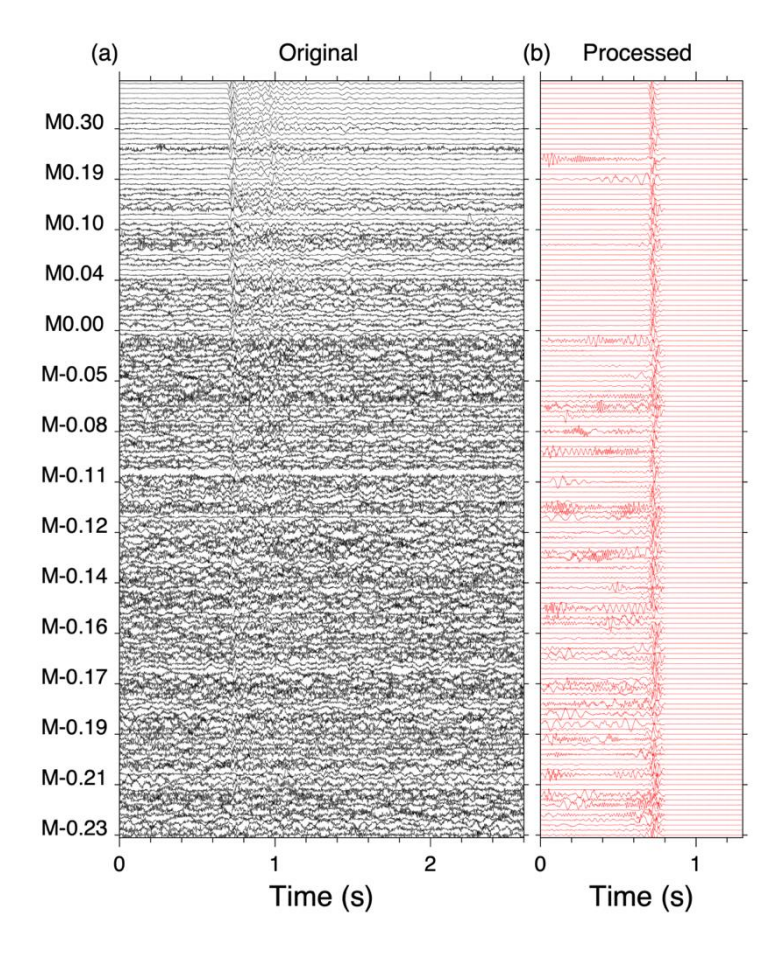


Figure 5: Comparison of *P*-wave signals at one of the surface nodal subarrays before (a) and after (b) signal processing in this study. The waveforms are sorted by magnitudes.

## ${\bf 3.3}\ Combining\ S\ urface\ and\ Downhole\ Arrays$

We apply MT inversion using FociMT (Kwiatek et al., 2016) based on a local 1-D velocity model to invert for double-couple MT solutions. The result using an example M0.38 event, for surface array data only, shows dominant strike-slip mechanism. The fault strike has an  $\sim$ N20°E trend, relatively well-constrained through 100 bootstrap-resampling steps (Figure 6). On the other hand, for downhole geophone data only, the inverted MT solution does not yield a reasonable solution because of poor azimuthal coverage (Figure 6). We further jointly invert for both surface and downhole array data. The inversion is parameterized with equal weight between the surface and downhole data, and the amplitudes from the surface data are scaled based on geometrical spreading to adjust for site response. Combining both surface and downhole data gives a more stable results from the bootstrapping process, where the fault strike pattern is slightly modified with a dominant N-S trend (Figure 6).

With the joint inversion scheme, we estimate the MT solutions for events that have more than 7 picks from the surface array. The results in Figure 7 show a prominent strike-slip mechanism throughout the seismically-active area. Fault strikes at northern part of the event cloud have a dominant trend of ~N30°E direction, and the southern part is prominent with a N-S trend. In general, the directional pattern

is comparable with the trend of earthquake distribution. To better evaluate the transition of fault strike pattern, we plan to resolve the MT solutions for smaller events based on waveform similarity analyses, which is an ongoing work.

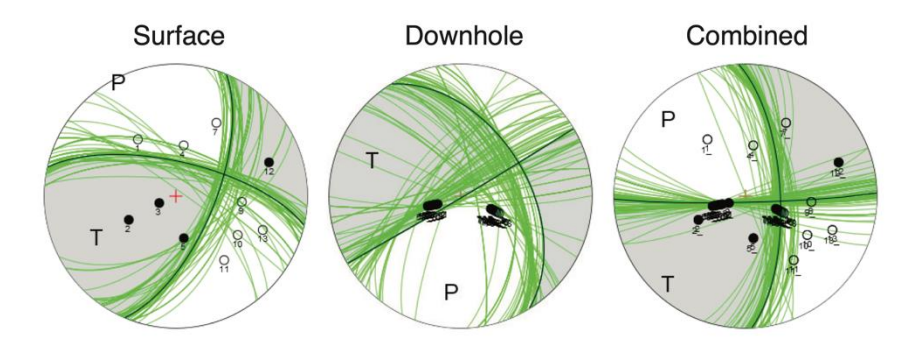


Figure 6: Double-couple moment tensor solutions shown as upper-hemisphere projection. The solutions are from 100 bootstrap steps, where each step has 5% of data are resampled with a reversed polarity. The bootstrap solutions of fault strikes are shown as green lines, where the green color represents a dominant strike-slip mechanism. White and black dots are the data with negative and positive polarity, respectively.

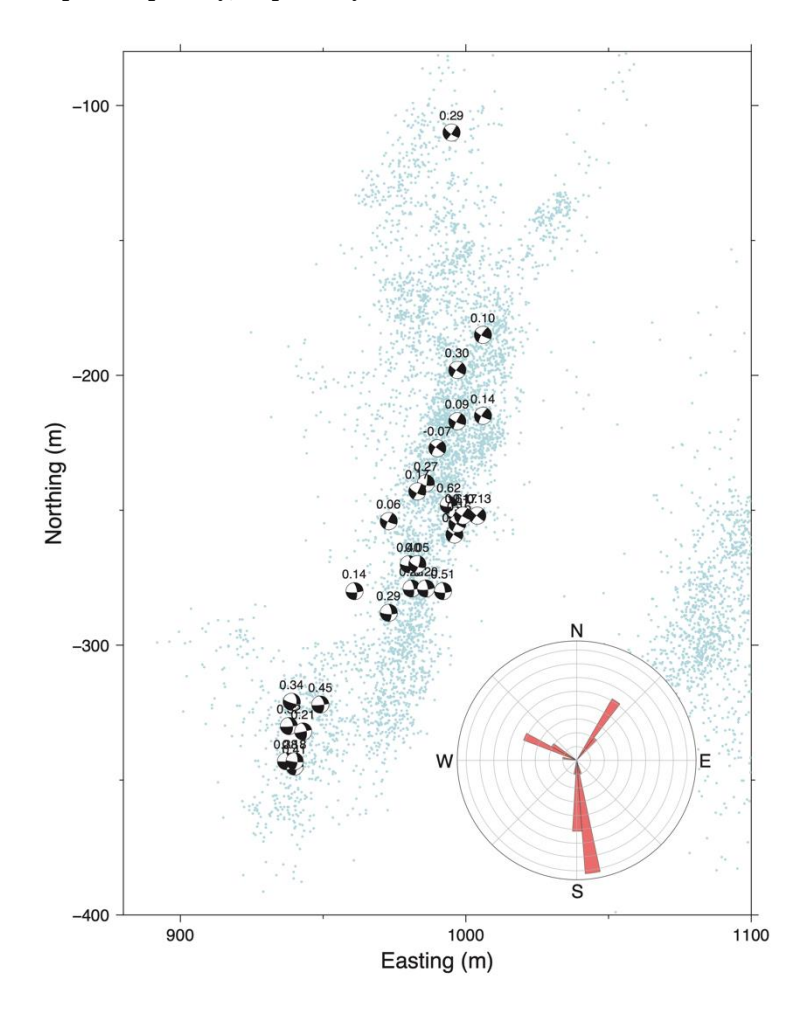


Figure 7: Moment tensor solutions combining both surface and downhole data. The presented events have at least 7 picks from the surface array. Their corresponding event magnitude are annotated. The beachballs are upper-hemisphere projection. The blue dots represent the microseismicity distribution from the stimulation, same as Figure 3c. The inset rose diagram shows the organization of fault strikes with a 10° interval. Note that there's 180° ambiguity from the moment tensor solution.

#### 4. CONCLUSIONS

We present our recent work for better characterizing microseismic events at Cape Modern, Utah, to prepare upcoming stimulation. The six new shallow subsurface seismometers have been deployed, and data are transmitted to EarthScope DMC. This seismometer network provides our backbone information of seismic monitoring. The velocity model is important for accurately estimate the location and moment tensor of earthquakes, and we develop the model based on existing velocity model at Utah FORGE, well log, and geology information. We will further update the velocity model once we record seismicity waveforms at the site.

To characterize subsurface stress, the moment tensor of microseismicity is important, but estimating it is not easy because of the low signal-to-noise ratio. We develop a method to invert moment tensors using both surface and borehole stations to increase the azimuthal coverage as well as the signa-to-noise ratio. Then we test this method to Utah FORGE 2022 stimulation data and estimate reliable moment tensors for around 30 earthquakes. They have similar moment tensor orientations, and we consider they are related to the direction of local stress field.

#### 3. ACKNOWLEDGEMENTS

We are grateful to Fervo Energy for their collaboration to this work and permission to present the results. This work is supported by the U.S. Department of Energy, Office of Energy Efficiency and Renewable Energy (EERE), Geothermal Technologies Office, under Award Number DE-AC02–05CH11231 with Lawrence Berkeley National Laboratory.

#### REFERENCES

- Dyer, B., Karvounis, D., Bethmann, F. (2023). Microseismic event catalogues from the well 16A(78)-32 stimulation in April, 2022 in Utah FORGE., ISC Seismological Dataset Repository, <a href="https://doi.org/10.31905/52CC4QZB">https://doi.org/10.31905/52CC4QZB</a>
- Helmholtz Centre Potsdam GFZ German Research Centre for Geosciences and gempa GmbH (2008). *The SeisComP seismological software package*. GFZ Data Services. doi:10.5880/GFZ.2.4.2020.003
- Chet Hopp, Taka'aki Taira, Michelle Robertson, Joseph J. Farrugia, Corinne Layland-Bachmann, Ernie Majer; Low-Noise Optical Accelerometers: Bridging the Gaps among Geophones, Accelerometers, and Broadbands in a Deep Borehole. Seismological Research Letters 2022;; 93 (4): 2367–2376. doi: https://doi.org/10.1785/0220210340
- Kwiatek, G., Martínez-Garzón, P., & Bohnhoff, M. (2016). HybridMT: A MATLAB/shell environment package for seismic moment tensor inversion and refinement. Seismological Research Letters, 87(4), 964-976.
- Ariel Lellouch, Nathaniel J. Lindsey, William L. Ellsworth, Biondo L. Biondi; Comparison between Distributed Acoustic Sensing and Geophones: Downhole Microseismic Monitoring of the FORGE Geothermal Experiment. *Seismological Research Letters* 2020; 91 (6): 3256–3268. doi: <a href="https://doi.org/10.1785/0220200149">https://doi.org/10.1785/0220200149</a>
- Nakata, N., Chang, J. P., Lawrence, J. F., & Boué, P. (2015). Body wave extraction and tomography at Long Beach, California, with ambient-noise interferometry. Journal of Geophysical Research: Solid Earth, 120(2), 1159-1173.
- Luca Scarabello, & Tobias Diehl. (2023). swiss-seismological-service/scrtdd: v1.8.0 (v1.8.0). Zenodo. https://doi.org/10.5281/zenodo.10063823
- Hao Zhang, Kristine L. Pankow, High-resolution Bayesian spatial autocorrelation (SPAC) quasi-3-D *Vs* model of Utah FORGE site with a dense geophone array, *Geophysical Journal International*, Volume 225, Issue 3, June 2021, Pages 1605–1615, <a href="https://doi.org/10.1093/gji/ggab049">https://doi.org/10.1093/gji/ggab049</a>
- Hao Zhang, Kristine Pankow, William Stephenson, A Bayesian Monte Carlo inversion of spatial auto-correlation (SPAC) for near-surface *Vs* structure applied to both broad-band and geophone data, *Geophysical Journal International*, Volume 217, Issue 3, June 2019, Pages 2056–2070, https://doi.org/10.1093/gji/ggz136